The pre-launch characterization of SIMBIO-SYS/VIHI imaging spectrometer for the BepiColombo mission to Mercury. I. Linearity, radiometry, and geometry calibrations

Gianrico Filacchione, Fabrizio Capaccioni, Francesca Altieri, Cristian Carli, Iacopo Ficai Veltroni, Michele Dami, Leonardo Tommasi, Gianluca Aroldi, Donato Borrelli, Alessandra Barbis, Marco Baroni, Guia Pastorini, and Raffaele Mugnuolo

Citation: Review of Scientific Instruments **88**, 094502 (2017); doi: 10.1063/1.4989968
View online: http://dx.doi.org/10.1063/1.4989968
View Table of Contents: http://aip.scitation.org/toc/rsi/88/9
Published by the American Institute of Physics

REVIEW OF SCIENTIFIC INSTRUMENTS **88**, 094502 (2017)

The pre-launch characterization of SIMBIO-SYS/VIHI imaging spectrometer for the BepiColombo mission to Mercury. I. Linearity, radiometry, and geometry calibrations

Gianrico Filacchione,[1,a)] Fabrizio Capaccioni,[1] Francesca Altieri,[1] Cristian Carli,[1] Iacopo Ficai Veltroni,[2] Michele Dami,[2] Leonardo Tommasi,[2] Gianluca Aroldi,[2] Donato Borrelli,[2] Alessandra Barbis,[2] Marco Baroni,[2] Guia Pastorini,[2] and Raffaele Mugnuolo[3]

[1]*INAF-IAPS, Istituto di Astrofisica e Planetologia Spaziali, via del Fosso del Cavaliere, 100, 00133 Rome, Italy*
[2]*Leonardo Company, via delle Officine Galileo, 1, 50013 Florence, Campi Bisenzio, Italy*
[3]*ASI Italian Space Agency, Centro di Geodesia Spaziale, 75100 Matera, Italy*

(Received 13 June 2017; accepted 7 September 2017; published online 29 September 2017)

Before integration aboard European Space Agency BepiColombo mission to Mercury, the visible and near infrared hyperspectral imager underwent an intensive calibration campaign. We report in Paper I about the radiometric and linearity responses of the instrument including the optical setups used to perform them. Paper II [F. Altieri *et al.*, Rev. Sci. Instrum. 88, 094503 (2017)] will describe complementary spectral response calibration. The responsivity is used to calculate the expected instrumental signal-to-noise ratio for typical observation scenarios of the BepiColombo mission around Mercury. A description is provided of the internal calibration unit that will be used to verify the relative response during the instrument's lifetime. The instrumental spatial response functions as measured along and across the spectrometer's slit direction were determined by means of spatial scans performed with illuminated test slits placed at the focus of a collimator. The dedicated optical setup used for these measurements is described together with the methods used to derive the instrumental spatial responses at different positions within the 3.5° field of view and at different wavelengths in the 0.4–2.0 μm spectral range. Finally, instrument imaging capabilities and Modulated Transfer Function are tested by using a standard mask as a target. *Published by AIP Publishing.* https://doi.org/10.1063/1.4989968

I. INTRODUCTION

Currently scheduled to be launched in 2018 with an expected arrival to the planet Mercury in late 2025, ESA's BepiColombo spacecraft will be the first European mission to explore the innermost planet of our Solar System.[1] The mission consists of two modular orbiters: a Mercury Planet Orbiter (MPO) provided by ESA and a Mercury Magnetospheric Orbiter (MMO) by the Japan Aerospace eXploration Agency (JAXA).[2] The two orbiters are carried and placed in orbit around Mercury by Mercury Transfer Module (MTM) that provides solar-electric propulsion. The integrated remote sensing suite of cameras and spectrometer SIMBIO-SYS (Spectrometer and Imagers for MPO BepiColombo-Integrated Observatory SYStem) is designed to achieve global mapping of Mercury's surface in high spatial resolution over a wide spectral range. The suite includes a High Resolution Imaging Channel (HRIC), a Stereo Imaging Channel (STC), and a Visible and near Infrared Hyperspectral Imager (VIHI). In this paper, we focus on the linearity, radiometry, and geometry responses characterization of the VIHI channel[3] accomplished at Leonardo Company, Campi Bisenzio (Florence, Italy) premises. The instrument spectral performance characterizations are discussed in Paper II.[4]

A summary of the VIHI optical design is given in Table I. The instrument employs a modified Schmidt telescope joined to a Littrow spectrometer with a flat grating. The spectrometer entrance slit is equipped with an electromechanical shutter: when it is commanded in closed position, the detector acquires internal background and dark current. The onboard software then automatically subtracts the dark current frame from successive scientific acquisitions before compressing and transmitting it on ground. The instrument's focal plane is a MCT 256 × 256 pixels array, with a pixel pitch of 40 × 40 μm and a full-well of 2 Me$^-$ by Raytheon Vision Systems. The detector is housed within a focal plane packaging that also includes an order sorting filter (variable high pass filter), a zero order light trap, a cold shield to reject parasitic light, and an active thermocooler (TEC), which is able to stabilize the detector at a nominal temperature of T = 220 K. The VIHI channel resolves the 0.4–2.0 μm spectral range with 256 spectral bands, a spectral sampling of 6.25 nm/band, and covers a Field Of View (FOV) of 64 mrad with 256 spatial pixels each having a 250 μrad Instantaneous Field Of View (IFOV). The instrument operates in pushbroom mode, acquiring a 25.6 km-wide swath on ground with 100 m/pixel resolution from a 400 km polar orbit by reaching a Signal to Noise Ratio (SNR) performance exceeding 100 for the majority of the observation scenarios as discussed in Sec. VI.

This paper is organized in several sections addressing specific arguments: the calibration setup used to acquire linearity and radiometric response data is described in Sec. II with a description of the associated dataset given in Sec. III. Section IV details the retrieval of the instrument radiometric

a)Email: gianrico.filacchione@iaps.inaf.it

TABLE I. VIHI optical parameters.

Parameter	Value	Units
Aperture	25	mm
Focal length	160	mm
f/number	6.4	N/A
Throughput (per pixel)	3.1×10^{-11}	m^2sr
FOV	64×0.25	mrad
IFOV (per pixel)	0.25×0.25	mrad
Scale	100	m/px from 400 km
Spatial samples	256	Number
Spectral bands	256	Number
Spectral dispersion	6.25	nm/band

response while the linearity response is given in Sec. V. Simulations of SNR expected at Mercury are given in Sec. VI. The measured reference signals and characteristics of the Internal Calibration Unit (ICU) sources are described in Sec. VII. The calibration setup used to characterize the geometry response and relative dataset is described in Sec. VIII. Section IX details the measurements of the instrument pixel and slit functions, while the characterization of the Field of View (FOV) is given in Sec. X. The acquisitions of the United States Air Force mask and analysis of the imaging capabilities are detailed in Sec. XI with the aim to derive the system MTF (Modulated Transfer Function).

II. LINEARITY AND RADIOMETRIC CALIBRATION SETUPS

During the calibration activities, a dedicated opto-mechanical modular setup has been used to perform measurements. Named OGSE (Optical Ground Support Equipment), this setup consists of an optical bench housing inter-chargeable light sources (monochromator, integrating sphere, and spectral sources), an autocollimating optical system, a focal plane target holder for test slits and pinholes, two inter-chargeable collimators, a steerable mirror mounted on two rotating mounts, and a reference spectroradiometer. All the OGSE elements are commanded by a dedicated computer via a Local Area Network (LAN). The VIHI optical head (OH) is mounted in a Thermo Vacuum Chamber (TVC) by means of a MGSE (Mechanical Ground Support Equipment) interface and kept at operative temperatures during the measurements: the focal plane is at a nominal temperature of 220 K (210–225 K is the expected range of variability during the observations at Mercury), while the mechanical structure is at a nominal temperature of 287 K (263 K is the minimum operative temperature). Thermal control is guaranteed by a heat pipe provided by the TVC and by an active Thermo Electric Cooler (TEC) mounted on the back of the detector. The TVC is housed above a rotating stage to allow the coalignment of the VIHI and OGSE boresights. The optical beam reaches the VIHI telescope entrance pupil through a CaF_2 window placed on the TVC wall. VIHI science and telemetry signals are acquired from the Proximity Electronics (PE) mounted on the same mechanical structure of the OH and housed in the TVC during the measurements. An EGSE (Electrical Ground Support Equipment) consisting of a power supply and a dedicated computer is used to communicate with the PE via a dedicated SpaceWire interface. The EGSE and OGSE are time-synchronized in order to command VIHI acquisitions only when the optical bench configuration has been reached. Each measurement is performed by executing telecommands included in an Automatic Test Procedure (ATP) that delivers them to VIHI through the EGSE and to the optical bench elements through the OGSE. Instrument science and telemetry data are visualized in real time and stored on the EGSE computer. Similarly, optical bench telemetry is stored on the OGSE computer. A schematic of the setup is shown in Fig. 1.

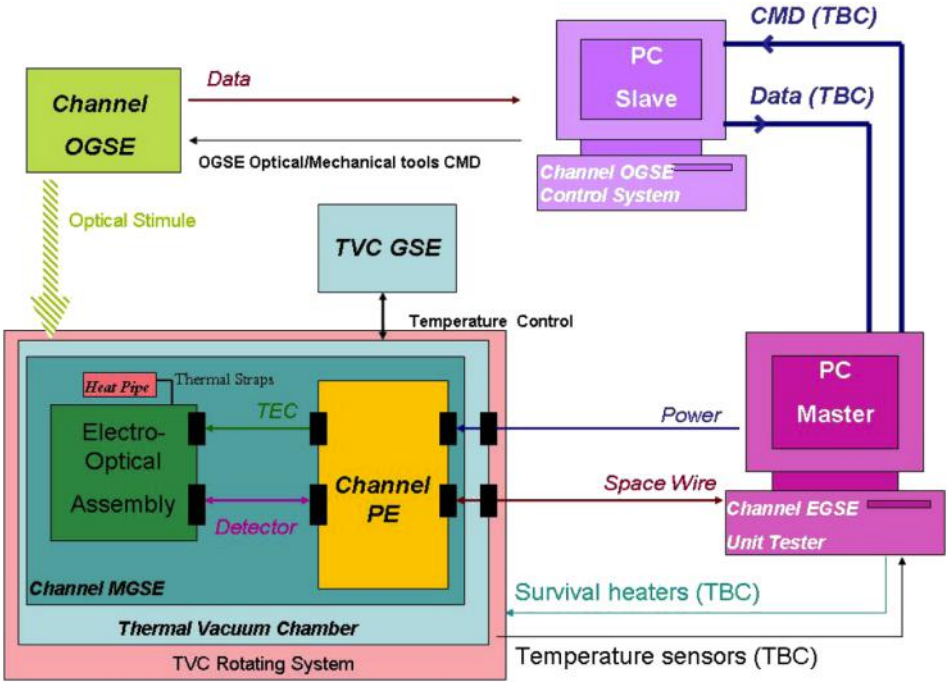

FIG. 1. VIHI calibration setup schematics showing OGSE and EGSE configuration.

TABLE II. VIS-IR collimator's optics characteristics.

Parameter	VIS	IR
Spectral range (μm)	0.4–1.0	1.0–2.1
Focal length (mm)	750	750
f/#	8.6	9.7
Diameter (mm)	87	80
Exit-working pupil max distance (mm)	480	500
FOV (deg)	±3.57	±1.8

The linearity and radiometric characterizations rely on a calibrated Integrating Sphere (IS) as a source. The sphere provides a diffused flat-intensity beam with calibrated radiance level, able to illuminate the full VIHI entrance pupil by means of the collimator. The sphere, a Labsphere model USS-2000-C, has a 50.8 cm diameter with a 20.3 cm diameter aperture, a 98% reflectance Spectraflect coating, three stabilized 35 W QTH lamps, one stabilized 100 W QTH lamp (provided with variable aperture shutter), and an internal photodiode to monitor the intensity of the output beam. The photodiode reading is used in feedback loop by the power supply to keep the lamp's current stabilized within ±0.1% level. The color temperature of the sources is 3000 K, and the maximum flux is 550 Wm^{-2} μm^{-1} sr^{-1} at $\lambda = 0.9$ μm. A N_2 line connected to the IS is kept active during the measurements to allow a continuous purging of the interior of the sphere with the aim to reduce the absorption of ambient water vapor and carbon dioxide along the optical path.

The full description and absolute radiometric/spatial characterization of the IS are given in Ref. 5. Two different achromatic lens-collimators are used to collimate the beam from sources to the VIHI pupil. In order to maximize the spectral transmittance, one collimator is optimized in the Visible (VIS) (0.4–1.0 μm) and another for the IR (1.0–2.1 μm) range. The characteristics of the collimators are given in Table II. The VIS collimator has a good transmittance in the 1–2.1 μm range but with poor spatial performances. Similarly, the IR collimator is not optimized to operate in the 0.4–1.0 μm range. However, it has high transmittance around 0.5 and 0.67 μm to allow optical alignments at visible wavelengths. This effect is particularly evident on the responsivity curves discussed later and shown in Figs. 4 and 5—bottom panels.

The OGSE setup for radiometric calibration is shown in Fig. 2, left panel. The set of measurements carried out with this OGSE configuration cover linearity vs. integration time, linearity vs. flux, and radiometric response. In order to relate the signal levels (in Digital Numbers, or DN) on VIHI FPA to the effective radiance at VIHI entrance pupil, each radiometric level output has been verified by measuring the spectral radiance produced by the entire OGSE chain consisting in the Integrating Sphere (IS), collimator, and Steering Mirror System (SMS) carried out with a calibrated spectroradiometer (ASD FieldSpec FR with 1° input optics, according to the configuration shown in Fig. 2, right panel). The ASD 1° FOV input optics is placed on the opposite side, with respect to the folding mirror, of the VIHI aperture, at 45° with respect to the collimator axis, and at the same distance in order to reproduce the optical path length up to the TVC window. These measurements are also used to monitor atmospheric absorptions by water vapor and carbon dioxide along the optical bench path that is in air. The FieldSpec FR spectroradiometer operates in the 0.35–2.5 μm spectral range using different detectors: a silicon detector for the 0.35–1.05 μm (VNIR) and two InGaAs detectors for the 0.95–2.5 μm (SWIR). The instrument spectral sampling is 1.4 nm with 3 nm of spectral resolution in the VNIR and 2 nm with 10–12 nm spectral resolution in the SWIR. According to the manufacturer, the radiometric calibration accuracy between 0.4 and 0.9 μm is ±5% rising to ±8% at 2.2 μm for operative temperatures between 10 °C and 30 °C. These performances have been verified by acquiring the flux

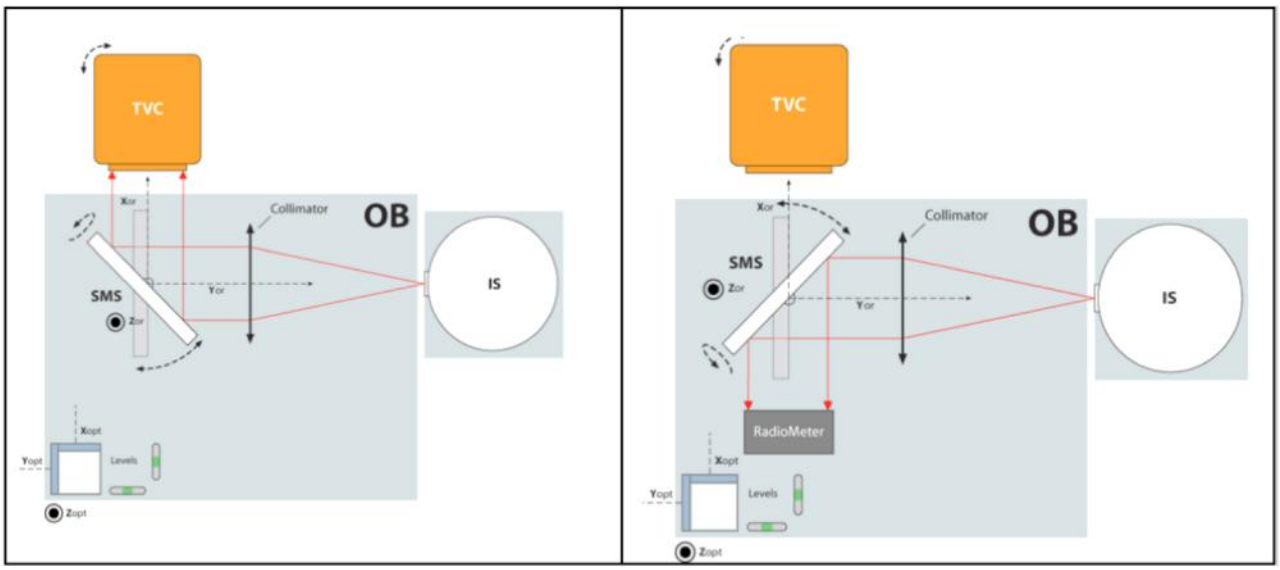

FIG. 2. Optical Bench (OB) setup for the linearity and radiometric calibration measurements. Left panel: configuration during VIHI measurements in which the Steering Mirror System (SMS) reflects the pupil of the integrating sphere towards VIHI instrument placed inside the Thermo Vacuum Chamber (TVC). Right panel: configuration during the radiometer acquisition of reference radiance from the IS. The position of the collimator is indicated in both cases.

from a stable, NIST traceable, radiance source following the specifications of the manufacturer.

III. RADIOMETRIC AND LINEARITY RESPONSE CALIBRATION DATASETS

The calibration dataset consists of two sets of measurements specific to the radiometric and linearity characterizations, coded in Table III as [R] and [L], respectively.

For the radiometric [R] measurements, several sessions are acquired by using the same setup but changing visible and infrared collimators: the corresponding sessions are identified with the codes CRNV and CRNI, respectively, in the session name. Four different output levels from the IS corresponding to a maximum radiance of 500, 380, 280, and 150 W m^{-2} μm^{-1} sr^{-1} at $\lambda = 0.98$ μm are measured and identified with the codes SPH4L, SPH3L, SPH2L, and SPH1L, respectively. In the SPH4L configuration, all the lamps are switched on, three 35 W lamps and one 100 W lamp; in SPH3L, three lamps are on, two 35 W and one 100 W; in SPH2L, two lamps are on, one 35 W and one 100 W; in SPH1L, one 100 W lamp is on. In addition to "Signal" (SIG) acquisitions of the IS flux, "Dark-Background" (BKG) acquisitions are taken while a cover blocks the collimator's entrance pupil in order to acquire detector's dark current and ambient background. These BKG measurements are subtracted from SIG data taken with the same integration time to remove the instrumental and ambient contribution from the signal. The integration times used for acquisitions are coded as "Short" (SRT) and "Long" (LNG). With SRT, we refer to integration times starting from the minimum settable time allowed by the proximity electronics of 68.5 μs, which can be used to measure the readout noise and includes other 99 times taken between 1.03 and 48 ms with an increment of 0.48 ms/step. The 200 LNG times are between 48.4 and 254.4 ms with an increment of 1.03 ms/step. For the linearity [L] measurements, the four different input radiance levels from the IS are used by acquiring ramps of integration times with an increment of

TABLE III. Radiometric [R] and Linearity [L] calibration session datasets.

Session name	#IS lamps on	Collimator	t_{exp}	No. steps	ms/step	Note
CRNVSPH4LSIGSRT	4	VIS	68.5 μs, 1.03–48 ms	100	0.48	IS signal [R]
CRNVSPH4LSIGLNG	4	VIS	48.4–254.4 ms	200	1.03	IS signal [R]
CRNVSPH3LSIGSRT	3	VIS	68.5 μs, 1.03–48 ms	100	0.48	IS signal [R]
CRNVSPH3LSIGLNG	3	VIS	48.4–254.4 ms	200	1.03	Signal
CRNVSPH2LSIGSRT	2	VIS	68.5 μs, 1.03–48 ms	100	0.48	IS signal [R]
CRNVSPH2LSIGLNG	2	VIS	48.4–254.4 ms	200	1.03	IS signal [R]
CRNVSPH1LSIGSRT	1	VIS	68.5 μs, 1.03–48 ms	100	0.48	IS signal [R]
CRNVSPH1LSIGLNG	1	VIS	48.4–254.4 ms	200	1.03	IS signal [R]
CRNVSPH1LBKGSRT	1	VIS	68.5 μs, 1.03–48 ms	100	0.48	IS dark/background [R]
CRNVSPH1LBKGLNG	1	VIS	48.4–254.4 ms	200	1.03	IS dark/background [R]
CRNISPH4LSIGSRT	4	IR	68.5 μs, 1.03–48 ms	100	0.48	IS signal [R]
CRNISPH4LSIGLNG	4	IR	48.4–254.4 ms	200	1.03	IS signal [R]
CRNISPH3LSIGSRT	3	IR	68.5 μs, 1.03–48 ms	100	0.48	IS signal [R]
CRNISPH3LSIGLNG	3	IR	48.4–254.4 ms	200	1.03	IS signal [R]
CRNISPH2LSIGSRT	2	IR	68.5 μs, 1.03–48 ms	100	0.48	IS signal [R]
CRNISPH2LSIGLNG	2	IR	48.4–254.4 ms	200	1.03	IS signal [R]
CRNISPH1LSIGSRT	1	IR	68.5 μs, 1.03–48 ms	100	0.48	IS signal [R]
CRNISPH1LSIGLNG	1	IR	48.4–254.4 ms	200	1.03	IS signal [R]
CRNISPH1LBKGSRT	1	IR	68.5 μs, 1.03–48 ms	100	0.48	IS dark/background [R]
CRNISPH1LBKGLNG	1	IR	48.4–254.4 ms	200	1.03	IS dark/background [R]
CRNVSPHTEXPTEST	4	VIS	68.5 μs, 1.0–200 ms	200	1.0	IS signal [L]
CRNVSPHTEXPTST3	3	VIS	68.5 μs, 1.0–250 ms	250	1.0	IS signal [L]
CRNVSPHTEXPTST2	2	VIS	68.5 μs, 1.0–300 ms	300	1.0	IS signal [L]
CRNVSPHTEXPTST1	1	VIS	68.5 μs, 1.0–350 ms	350	1.0	IS signal [L]
CDCXDRK	n.a.	n.a.	68.5 μs, 10.0–500 ms	19	10 (0÷100 ms)	Dark current [L]
					50 (100÷500 ms)	At T = 210.1 K
CDHXDRK	n.a.	n.a.	68.5 μs, 10.0–250 ms	14	10 (0÷100 ms)	Dark current [L]
					50 (100÷250 ms)	At T = 225.0 K
CDNXDRK	n.a.	n.a.	68.5 μs, 10.0–150 ms	19	10 (0÷100 ms)	Dark current [L]
					25 (100÷150 ms)	At T = 219.9 K

1 ms/step between readout time and increasing upper limits of 200, 250, 300, and 350 ms for the SPH4L, SPH3L, SPH2L, and SPH1L configurations, respectively. By decreasing the flux and using longer integration times, we explored the dynamical range up to saturation. These measurements correspond to sessions named CRNVSPHTEXPTEST, CRNVSPHTEXPTST3, CRNVSPHTEXPTST2, and CRNVSPHTEXPTST1. Finally, the linearity of the dark current at the three detector's operative temperatures is measured in sessions CDCXDRK (detector T = 210.1 K, cold temperature case), CDHXDRK (T = 225.0 K, warm case), and CDNXDRK (T = 219.9 K, nominal case) where different integration times ramps were commanded to characterize the detector's dark current between readout and saturation.

IV. RADIOMETRIC RESPONSE

By comparing the instrumental raw DN with a reference input radiance for a given integration time, it is possible to determine the conversion factor or the instrument response function (in DN m^2 sr μm W^{-1} s^{-1}).[6] A similar approach has been successfully used for similar imaging spectrometers in the past.[7] The input radiance is given by different flux levels from an integrated sphere, settable to reproduce the expected radiance levels for the mission around Mercury. The instrument has been operated with typical integration times, from 68.5 μs to 0.5 s in order to match operative conditions. Many averages with different combinations of input radiances and integration times have been acquired together with the corresponding dark and background frames necessary to remove detector's dark current plus ambient and instrument background. After having verified the spatial uniformity of the integrating sphere flux across the FOV, the instrument responsivity has been determined for each pixel of the detector by following the methodology discussed hereafter. VIHI responsivity $R(s,\lambda)$ on sample s and wavelength λ is computed as

$$R(s,\lambda) = \frac{DN(s,\lambda)}{S(\lambda)\cdot\tau(\lambda)\cdot t}, \quad (1)$$

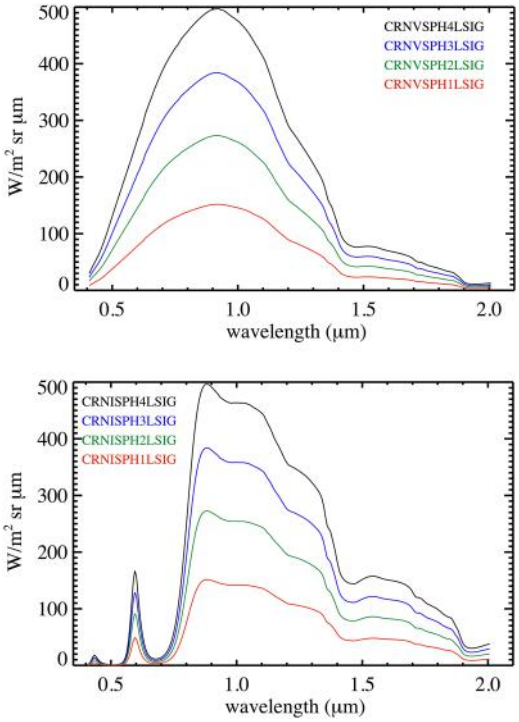

FIG. 3. Spectral radiance emitted by the IS as measured by the FieldSpec spectroradiometer as in configuration shown in the right panel of Fig. 2 through the VIS collimator (top panel) and IR collimator (bottom panel) for the four flux settings (from four to one lamps switched on). The setup settings are reported in Table III.

where the signal in DN is the difference between the signal measured on the IS and the background measured by shutting the IS aperture at the same integration time t. The radiance S emitted by the IS is measured by the FieldSpec spectrophotometer and is shown in Fig. 3 for each of the four flux levels with the VIS and IR collimator setups. With respect to these values, the radiance measured by VIHI is further attenuated by the TVC CaF_2 optical window transmittance $\tau(\lambda)$. In the following, we are assuming the VIHI spectral response discussed in Ref. 4 that enabled us to assign the central wavelength (λ) and the spectral response function ($\Delta\lambda$) for each band (b). For

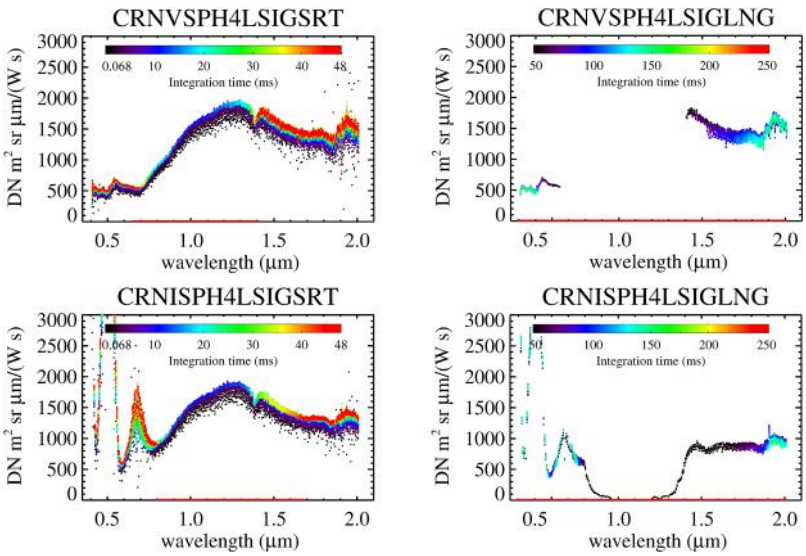

FIG. 4. Variability of the responsivity measured on sample = 128 (slit's center) for short integration times (t = 68.5 μs, 1.03–48 ms, left column) and for long integration times (t = 48.4–254.4 ms, right column). Measurements made with maximum radiance input (IS with four lamps switched on, corresponding to 500 W m^{-2} μm^{-1} sr^{-1} at λ = 0.98 μm) with the VIS (top panel) and IR collimator (bottom panel). Saturation counts are filtered to 0. The VIS sessions are representative for the spectral range $\lambda < 1$ μm while the IR sessions must be considered for $\lambda > 1$ μm.

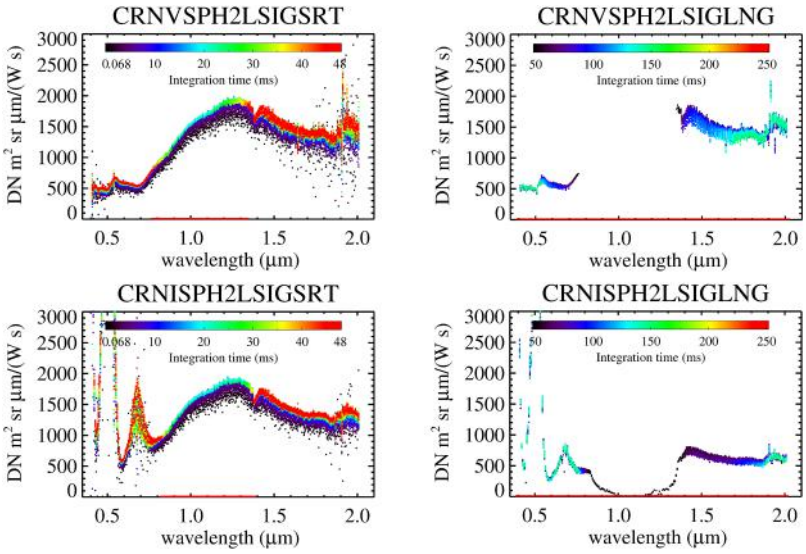

FIG. 5. Same as Fig. 4 but for intermediate radiance input (IS with two lamps switched on, corresponding to 280 W m^{-2} μm^{-1} sr^{-1} at $\lambda = 0.98$ μm).

convention, the minimum wavelength (≈0.4 μm) corresponds to band = 256 and maximum (≈2.0 μm) to band = 1.

The radiances shown in Fig. 3 are obtained by averaging 10 IS measurements performed by the spectroradiometer before and 10 after each VIHI measurement, then resampled on VIHI spectral range and response. The VIHI saturation limit is set at $DN_{sat.} = DN_{IS} - DN_{BKG} \geq 8000DN$. These pixels are flagged at value 0 in Figs. 4 and 5 where the responsivity curves for the integration times reported in Table III are shown. The responsivity curves derived for both short and long integration time series and maximum radiance input (IS with four lamps switched on, corresponding to a maximum radiance of 500 W m^{-2} μm^{-1} sr^{-1} at $\lambda = 0.98$ μm) are shown in Fig. 4. As shown in Fig. 4—top left panel—with the maximum IS flux, the VIS (0.4–1.0 μm) signal is completely unsaturated up to integration time of about 12 ms. Longer integration times, up to 48 ms, are used to improve the signal to noise ratio in the 0.4–0.65 μm range where the response is low due to the overall VIHI optical efficiency. Similarly, in the IR (1.0–2.0 μm) range (bottom left panel), the signal is unsaturated up to integration time of about 12 ms, while longer integration times up to 48 ms can be used to improve the signal in the 1.7–2.0 μm range. On both VIS and IR sessions when the signal is not saturated nor it is too low, like for the shorter times, the responsivity curves for different integration times are grouped together. This behavior indicates that the instrument's spectral response does not change within the linear response regime.

Keeping the same maximum IS flux and using the long integration times (48.4–254.4 ms) are possible to explore the variability of the responsivity at the two extremes of the spectral range where the instrument response is lower while it is saturating more and more bands in the middle of the spectral range, where the response is higher, when the integration time increases. The resulting curves are shown in Fig. 4—right column. In these cases, it is possible to follow the changes occurring in the responsivity when the integration time increases above 48.4 ms. Since the pixels are

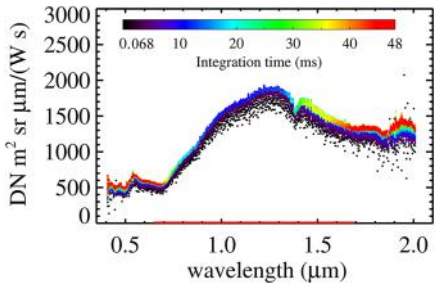

FIG. 6. Instrument responsivity at the slit's center (optical boresight, sample = 128) derived for short integration times after bridging VIS CRNVSPH4LSIGSRT and IR CRNISPH4LSIGSRT sessions at 1 μm. Saturation counts are filtered to 0.

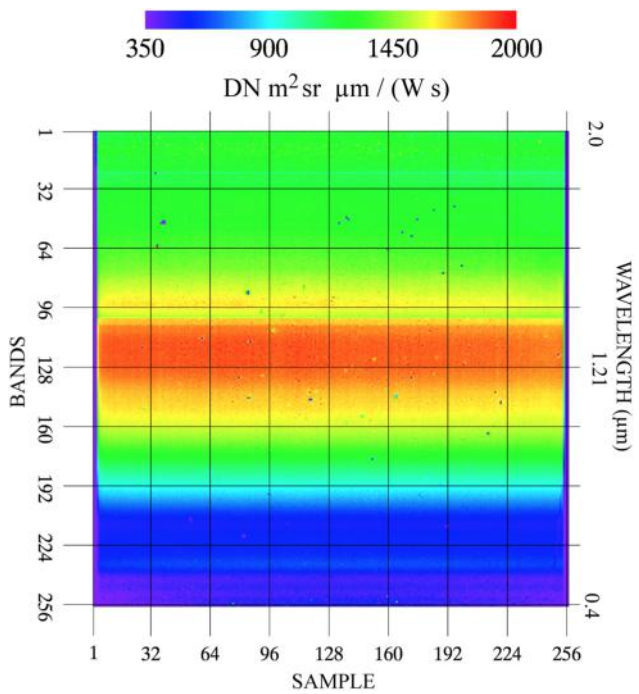

FIG. 7. VIHI Instrument Transfer Function ITF array derived for integration time t = 10 ms from CRNVSPH4LSIGSRT and CRNISPH4LSIGSRT sessions.

progressively approaching to saturation, the response loses linearity, resulting in a decrease of the responsivity. This effect is evident for the VIS acquisitions shown in the top right panel where responsivity drops from t = 48.4 (black points) to about 150 ms (cyan-green points) before reaching saturation. A similar trend is also seen in the IR acquisition reported in the bottom right panel. The changes occurring in the response for similar integration times but with lower IS flux (2 lamps switched on, corresponding to a maximum radiance of 280 W m^{-2} μm^{-1} sr^{-1} at $\lambda = 0.98$ μm) are shown in Fig. 5.

By halving the input flux from the IS, the responsivity does not change, as expected. Moreover, since the flux is lower, the stability of the response for longer integration times can be estimated because the saturation limit is reached later and on a minor number of spectral channels. In fact, the signal is completely unsaturated up to about 20 ms with respect to 12 ms of the maximum flux case.

The two responsivity curves measured with the VIS and IR collimators for the short integration times (68.5 μs–48 ms) are bridged at 1 μm in order to retrieve the complete responsivity across the entire spectral range. Figure 6 shows the resulting curves obtained by using the VIS collimator measurements for data within $0.4 \leq \lambda \leq 1.0$ μm and the IR collimator for $1.0 \leq \lambda \leq 2.0$ μm.

The results shown up to here refer to the pixel placed at the center of the slit corresponding to the optical boresight at sample = 128. In order to extend the responsivity to the whole focal plane, we rely on the fact that the IS illuminated pupil is highly spatially homogeneous at each wavelength. As measured by Ref. 5, the emitted radiance has a spatial uniformity equal to 99.2% for the SPH4L and SPH3L cases, 99.1% for the SPH2L case, and 97.9% for the SPH1L case. Within these limits the VIHI slit can be considered uniformly illuminated, allowing us to derive the Instrumental Transfer Function (ITF) array for each pixel of the detector by repeating the previous analyses for all 256 samples. The resulting ITF derived from SPH4L measurement with t = 10 ms is shown in Fig. 7.

V. LINEARITY RESPONSE

The linearity response of the instrument's detector has been characterized by keeping the same setup used for the radiometric calibration previously described but changing the sequence of integration times. Four sessions, one for each IS flux level, are executed. The sequences consist of a series of acquisitions of the IS signal taken with the VIS collimator and with integration times going from t = 68.5 μs, 1.03 ms to 200, 250, 300, 350 ms, 1 ms/step increment, for IS radiances of 500, 380, 280, 150 W m^{-2} μm^{-1} sr^{-1} at $\lambda = 0.98$ μm, respectively. The sessions, named CRNVSPHTEXPTEST to CRNVSPHTEXPTST1, are listed in Table III. Figure 8 shows the signal ramps extracted at boresight for different spectral bands with the four IS flux levels. In all four cases, the ramps are

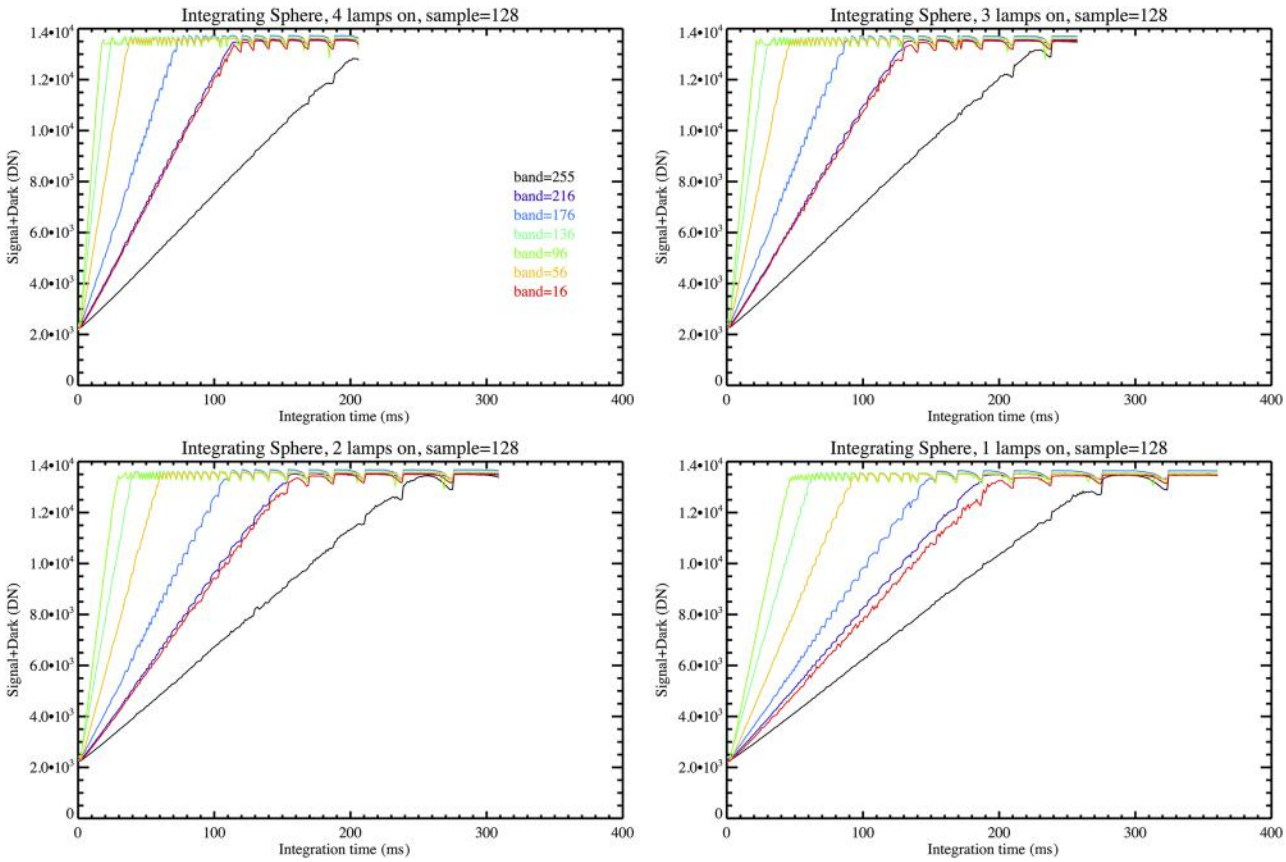

FIG. 8. Linearity response measured with the four flux levels from IS (decreasing from four to one lamp switched on top left to bottom right panels) boresight on different bands (from 16 to 255). The "bumps" visible on the curves are due to a readout effect explained in the text. Saturation occurs when signal plus dark is beyond 13 200 DN.

remarkably linear between the shortest useful integration time (t = 1.03 ms) up to the proximity of the saturation that occurs for a level of 13 200 DN. For a given IS flux level, the different slopes are correlated with the instrumental response that is not constant across the spectral range: thus, at the maximum values of the responsivity (at the middle of the spectral range, see Fig. 7), the ramps have the maximum slope (bands 96 and 136). Conversely, at the two spectral extremes, the response is lower resulting in ramps with more gentle slopes (bands 16, 216, and 255). By reducing the IS flux from 4 to 1 lamp switched on, we observe, as expected, a reduction of the slope's values with the signal reaching saturation at longer integration times. The linearity of the ramps is kept in all cases. The series of "bumps" visible on all curves and spaced with frequency increasing towards the shortest integration times are due to a readout effect: since the EGSE is not permitting a dynamical change of the repetition time between successive acquisitions while the integration time is indeed changing, it could occur for some combinations of these two parameters that the proximity electronics commands a reset of the focal plane while the readout is occurring, resulting in a small bias in the signal. While this effect cannot happen in flight conditions where the instrument shall operate with a constant set of repetition and integration times, a similar behavior cannot be avoided for this kind of characterization given the limitations of the EGSE. However, the presence of this bias on some acquisitions does not preclude the analysis of the linearity response.

By using the range of integration times for which the signal is not saturated ($\approx 2200 \leq DN \leq 13\,200$ DN), it is possible to compute the best fit lines to the signal ramps taken on the same pixel for the four different input radiance values, as shown in the left column of Fig. 9. The ratios between the measured signal and the best fit values for two cases (bands 16 and 176) are shown in the right column. The linearity of the response is typically at ±2% level, including the fluctuations caused by the readout effect. In general, the detector is less linear at the two extremes of the dynamical range: at short integration times ($t \leq 5 \div 10$ ms) where the signal is low, we observe an increase in the ratios, up to 10% level for both spectral channels. Moving towards the saturation limit, all ratio curves decrease to a 5% level. This loss of linearity at low and high fluxes is expected and is within the scientific requirements.

The VIHI detector is designed to operate at a nominal temperature T_{nom} = 220 K with a possible excursion between T_{cold} = 210 K and T_{warm} = 225 K. This range has been foreseen by the instrument thermal model that takes into account the temperature variations occurring onboard the BepiColombo spacecraft during the different phases of the mission around Mercury. Despite the detector being cooled and stabilized by an active TEC mounted in thermal contact, it is not possible to

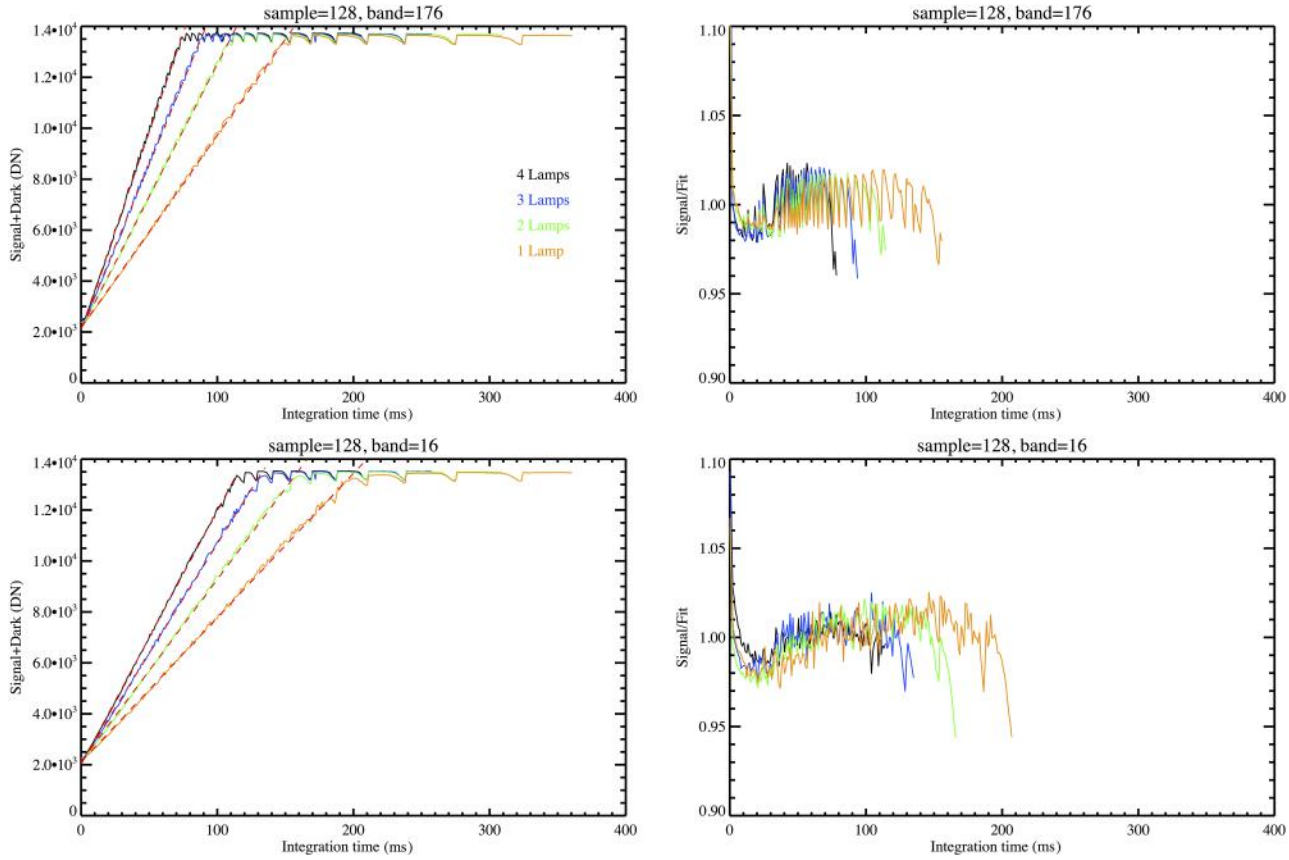

FIG. 9. Left panels: linear fits (red dashed lines) computed on the signal plus dark DNs for pixel sample = 128 (boresight) and bands 176 (top) and 16 (bottom) for the four IS fluxes. Right panel: ratios of the signal/fit for the two cases. The "bumps" visible on the curves are due to a readout effect explained in the text. Saturation occurs when signal plus dark is beyond 13 200 DN.

keep $\Delta T \geq 40$ K between the detector and the heat-pipe interface provided by the spacecraft to dissipate the TEC power. Since the dark current is highly dependent on the detector temperature, it is necessary to characterize it within the range of expected temperatures. The detector's temperature has been changed to the three values (T_{cold}, T_{nom}, T_{warm}) by operating on the TEC set point. The temperature of the instrument mechanical structure has been maintained at nominal temperature (278.1–278.4 K). The dark current sessions acquired for each temperature are reported in Table III where the integration times commanded for each step are also indicated. For the three detector's temperatures, a ramp of increasing integration times is acquired, by repeating each acquisition 50 times in order to improve statistics. These measurements are performed by closing the TVC optical window with a light-tight cover in order to maintain the instrument entrance pupil in complete darkness. Figure 10 shows the median trends of the dark current measured on all pixels as a function of the integration time. The dark current values confirm a linear trend, as already seen before on the linearity measurements performed with the IS. In the figure, the results of a linear fit performed on the dark current data are also reported. The offset, corresponding to the dark value extrapolated at null integration time, is slowly increasing from 2150.48 DN to 2160.58 up to 2169.52 DN for detector's temperatures of T_{cold} = 210.1, T_{nom} = 219.9, and T_{warm} = 225.0 K, respectively. It is therefore scarcely dependent on temperature changes. Conversely, the dark current rate has a strong dependence on the operative temperature of the detector, increasing from 12.29 to 40.29 up to 72.55 DN/ms for the temperature values reported before. This trend of the dark current imposes operability restrictions in the range of possible integration times available for scientific observations: in the warm case, the entire full well of the detector is saturated by the dark current at integration times longer than ≈130 ms. In the nominal case, a similar condition occurs at ≈260 ms. On the contrary, the lower dark current rate occurring in the cold case allows to avoid saturation even with long integration times: at 500 ms, the dark current is at about 8000 DN.

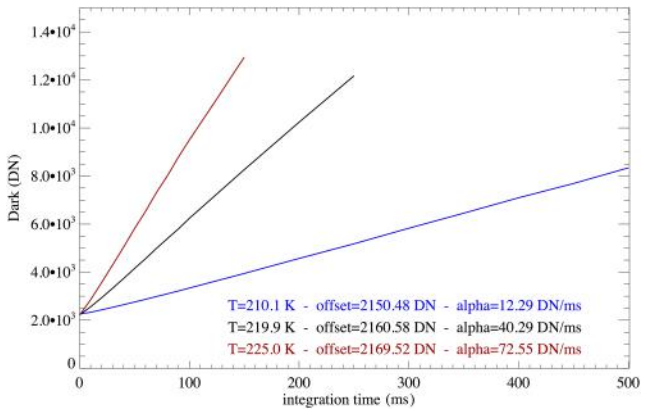

FIG. 10. Median dark current values measured on the entire set of pixels for cold (T_{cold} = 210.1 K), nominal (T_{nom} = 219.9 K), and warm (T_{warm} = 225.0 K) detector's temperature cases. The offset and dark current rate (alpha) calculated by means of a linear fit are shown for each case. Detector's saturation occurs at about 13 200 DN.

VI. RADIOMETRY SIMULATIONS FOR MERCURY OBSERVATIONS

In this section, we report about the simulations of the expected SNR of the VIHI instrument when operating at Mercury. According to the original BepiColombo mission plan, the MPO spacecraft will be placed on an elliptical inertial polar orbit with a periherm altitude of 400 km and apoherm of 1500 km and an orbital period of about 2.3 h.[3] As a consequence of the mission launch delay, a different orbit is currently under study. However, for the evaluation of the VIHI radiometric performances, we are adopting here the observation cases relative to the original scenario. The high orbital eccentricity (e = 0.206) of Mercury causes a large change in the heliocentric distance that varies between 0.31 AU at perihelion (true anomaly TA = 0°) to 0.47 AU at aphelion (TA = 180°). This corresponds to a variation of the input radiance by a factor of 2.3 between aphelion and perihelion. Further changes of the radiance are expected during the day side arc of the orbit where the radiance is varying with the sub-spacecraft latitude.

The simulations are performed by using the measured VIHI responsivity and dark/background values. We report about the results obtained with a fixed integration time of t = 30 ms. The selection of this average integration time is the result of the dwell time variability estimated from orbital analysis. The dwell time (t_{dwell}), defined as the time necessary to move the projection of one pixel on the surface by one IFOV, depends on instrumental IFOV value, spacecraft distance (D), and subspacecraft point velocity (v_{sub}) according to the equation,

$$t_{dwell} = \frac{IFOV \cdot D}{v_{sub}} \quad (2)$$

In case of VIHI, the dwell time is changing between 40 ms when Mercury is at aphelion (TA = 180°) and the MPO is at periherm on the equator, to about 280 ms when Mercury is at perihelion (TA = 0°) and the MPO is at apoherm on equator. Assuming a maximum integration time equal to 0.25 times the dwell time to avoid smearing, these conditions correspond to t_{exp} equal to 10 and 50 ms, respectively. This is to justify our choice to include here the results for the average t_{exp} = 30 ms value.

Apart from setting the integration time, we have performed SNR simulations assuming two different albedo

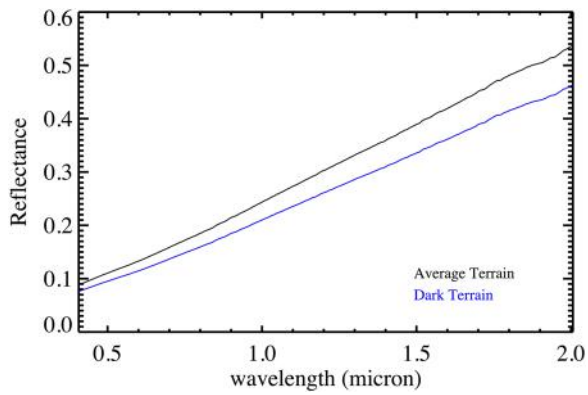

FIG. 11. Mercury average (ρ_{avg}) and low albedo (ρ_{low}) terrain reflectances used as an input for SNR simulations.

values to model surface radiance: (1) an average albedo terrain modeled as an anorthitic mixture with reflectance $\rho_{avg}(0.55\ \mu m) = 0.12$ and (2) a low albedo terrain simulated by scaling the previous one to $\rho_{low}(0.55\ \mu m) = 0.105$ (see Fig. 11).

For a given point at latitude (lat) on the surface of Mercury, the illumination conditions change along the orbit according to the solar zenith angle (ZA),

$$ZA = a\ \cos(\cos(lat) \cdot abs(\cos(\pi - TA))), \tag{3}$$

consequently, the spectral radiance S(λ) of diffusely reflected solar radiation emanating from Mercury's surface is given by

$$S(\lambda) = \cos(ZA) \cdot \rho(\lambda) \frac{SI(\lambda)}{\pi \cdot D_{Sun}^2}, \tag{4}$$

where $\rho(\lambda)$ is the surface reflectance (from cases shown in Fig. 11), $SI(\lambda)$ is the solar irradiance measured at 1 AU from Ref. 8, and D_{Sun} is the heliocentric distance (in AU). The VIHI expected signal, in DN, is calculated from Eq. (1) for a given sample(s),

$$DN(\lambda) = S(\lambda) \cdot R(\lambda) \cdot t_{\exp}. \tag{5}$$

Finally, the SNR ratio is computed as

$$SNR(\lambda) = \frac{DN \cdot \eta}{\sqrt{DN \cdot \eta + DN_{bkg} \cdot \eta}}, \tag{6}$$

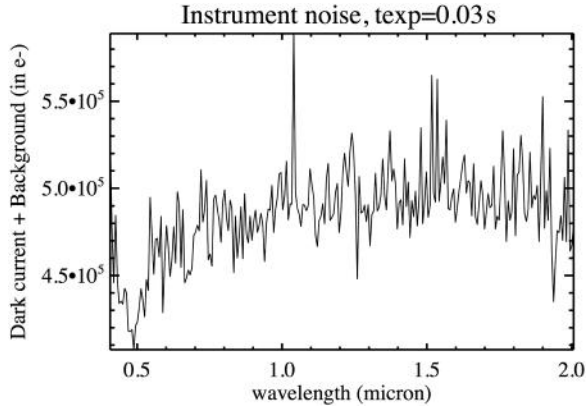

FIG. 12. VIHI dark current and background measurement (converted in photoelectrons) taken with integration time of $t_{\exp}$ = 30 ms.

where $\eta = 146\ (e^-/DN)$ is the A/D converter factor allowing to convert DN in photoelectrons and is determined by scaling the detector's full well capacity (2 Me$^-$) for the dynamical range used by the A/D converter (≈14 000 DN). The background and dark current photoelectrons measured during the radiometric calibration session with a $t_{\exp}$ = 30 ms are shown in Fig. 12.

The four more extreme observation cases are considered for the SNR simulation:

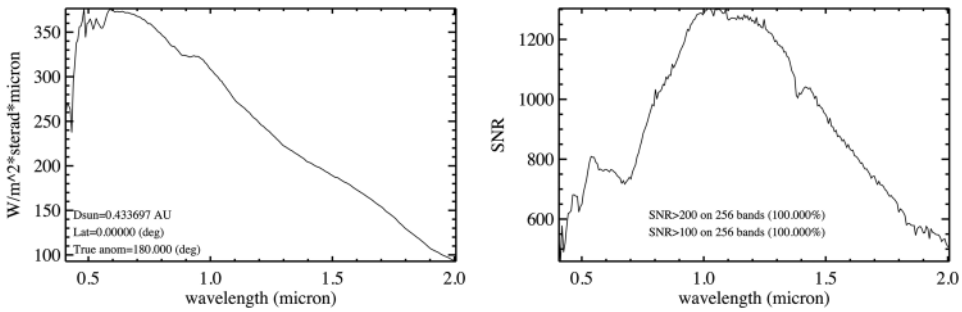

FIG. 13. Expected spectral radiance for Mercury average albedo terrain (left panel) and instrumental SNR (right panel) for case 1 with $t_{\exp}$ = 30 ms.

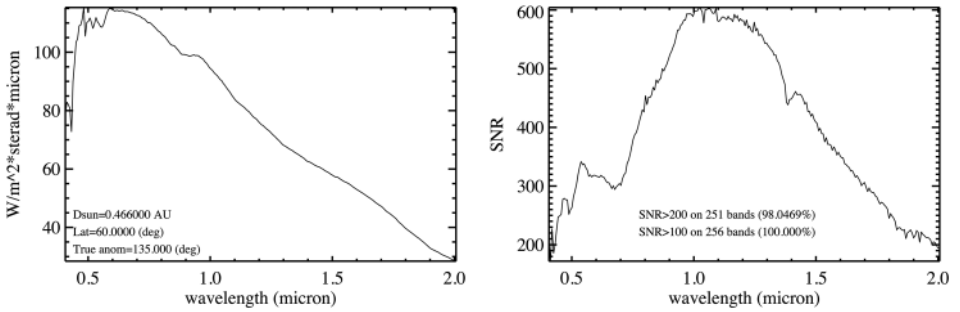

FIG. 14. Expected spectral radiance for Mercury average albedo terrain (left panel) and instrumental SNR (right panel) for case 2 with $t_{\exp}$ = 30 ms.

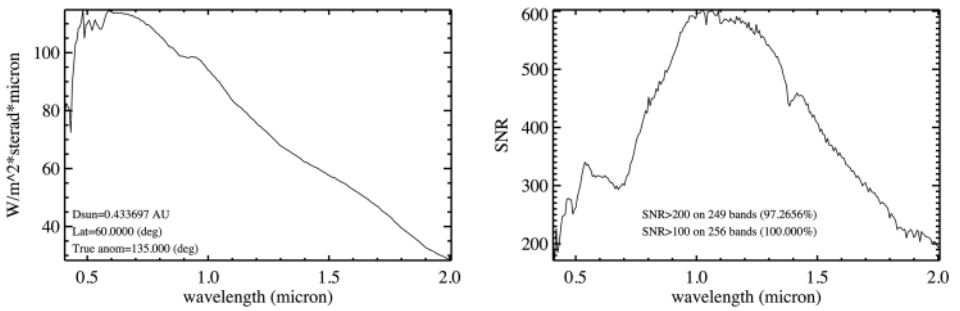

FIG. 15. Expected spectral radiance for Mercury low albedo terrain (left panel) and instrumental SNR (right panel) for case 3 with $t_{\exp}$ = 30 ms.

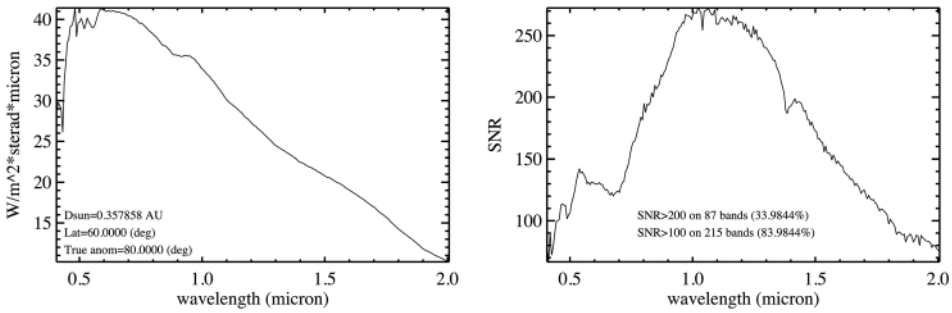

FIG. 16. Expected spectral radiance for Mercury low albedo terrain (left panel) and instrumental SNR (right panel) for case 4 with t_{exp} = 30 ms.

1. sub-spacecraft latitude = 0°, TA = 180°, Mercury average albedo terrain (see Fig. 13);
2. sub-spacecraft latitude = 60°, TA = 135°, Mercury average albedo terrain (see Fig. 14);
3. sub-spacecraft latitude = 60°, TA = 135°, Mercury low albedo terrain (see Fig. 15);
4. sub-spacecraft latitude = 60°, TA = 80°, Mercury low albedo terrain (see Fig. 16).

The resulting SNR is always ≥200 for all the simulated scenarios with the exclusion of a few channels at the two spectral extremes of the range for the case 4 where it is <100. This case, however, is not particularly critical because here it is possible to increase the integration time to achieve the desired SNR.

VII. INTERNAL CALIBRATION UNIT REFERENCE SIGNAL

The VIHI Internal Calibration Unit (ICU) design is detailed in Ref. 3. It consists of two sources: an incandescent lamp and a Light Emitting Diode (LED) with a dedicated optical system that is able to project a fraction of the emitted flux within the telescope FOV. The white LED is optimized for the 0.4–0.8 μm spectral range while the incandescent lamp, for the 0.7–2.0 μm range. The LED by NICHIA (model NJSW036) has a flux of 62 lumens when powered at 1.8 W (450 mA and 3.6 V). The lamp by HPX-Welch Allyn (model 01163)

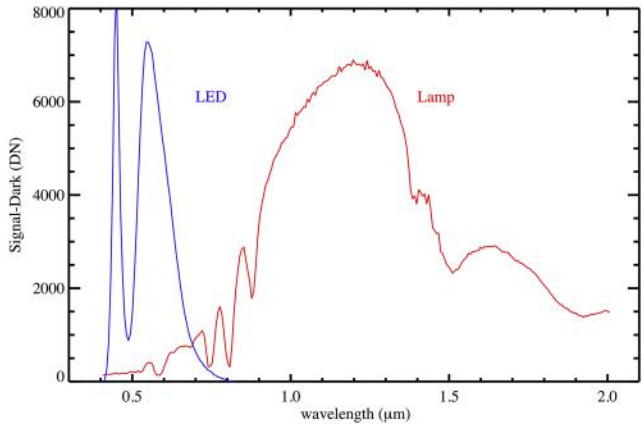

FIG. 17. VIHI internal calibration unit reference spectral signals from LED and lamp at boresight (s = 128).

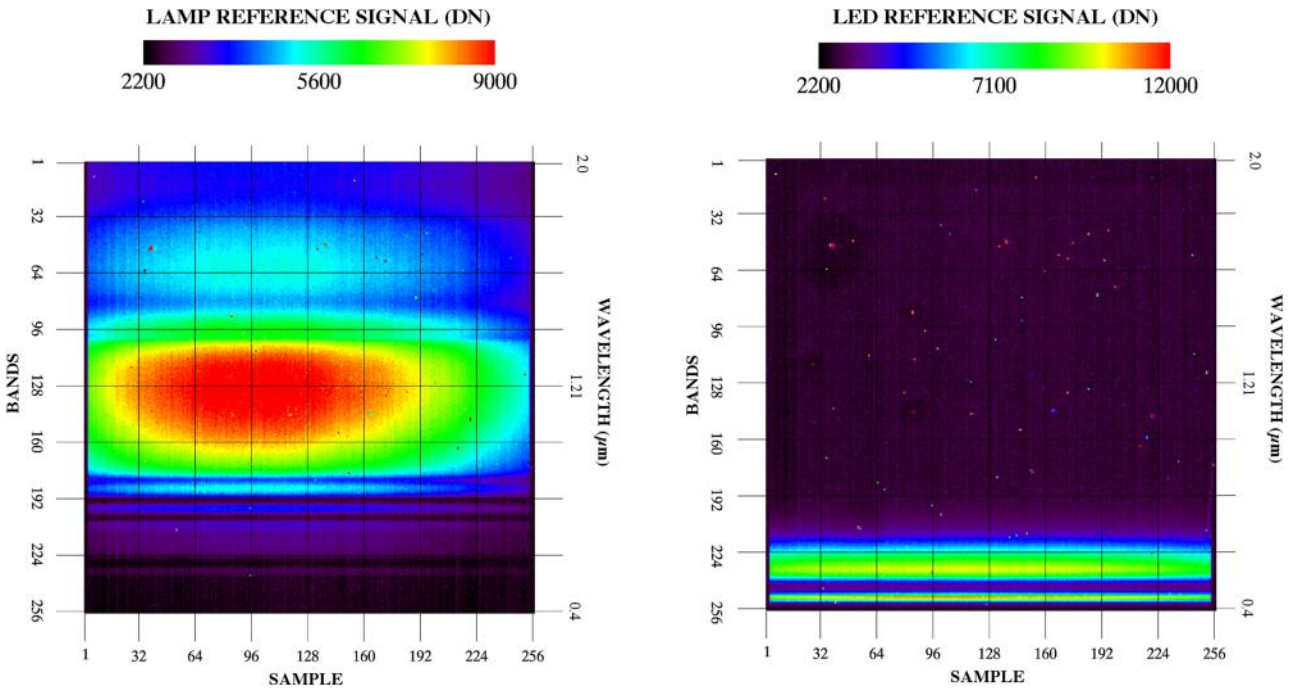

FIG. 18. Distribution of the VIHI internal calibration unit reference signals from LED and lamp across the focal plane.

has a color temperature of 3035 K when powered at 2.5 W (500 mA and 5 V). Both sources have sustained extensive qualification to be used in space environment. A didymium filter, placed close to the lamp's bulb, introduces reference absorption features at specific wavelengths that are used to check the spectral response of the instrument. The two sources are powered by stabilized currents in order to guarantee a constant flux. In this way, it is possible to check the temporal stability of the instrumental radiometric response and relative variations across the spectral range. The sources are switched-on in succession and acquired separately. As shown in Fig. 17, the white LED signal is characterized by two strong emission peaks at λ = 0.451 and 0.551 μm separated by a minimum at λ = 0.488 μm. The IR lamp signal is continuous with the principal absorption features by didymium filter recognizable at λ = 0.739, 0.808, 0.877, and 1.5 μm. These features can be used to verify the spectral response stability. While the ICU signals are not completely uniform across the focal plane (Fig. 18), it is nevertheless possible to use them to verify pixel-to-pixel variations useful to keep track of single defective pixels or clusters of them.

VIII. GEOMETRY RESPONSE CALIBRATION SETUP AND DATASET

To perform the geometric response calibration, a set of suitable targets (test slits of various sizes and USAF mask illuminated in transmission) are placed in the OGSE focal plane. The collimated beam from the OGSE is then oriented in the VIHI FOV by means of Steering Mirror System (SMS) according to the required directions for the measurement to be carried out. The SMS mechanism allows controlling the mirror movements in azimuth (AZ) and elevation (EL) angles. The SMS AZ angle is oriented perpendicular to the VIHI slit and allows scanning along the line direction. The EL angle is along the VIHI slit direction allowing a scan along the sample direction. The OGSE target is imaged on the VIHI entrance slit (and relayed, after dispersion, on VIHI FPA) with a magnification ratio depending on the ratio between VIHI and collimator focal lengths,

$$MR = \frac{F_{VIHI}}{F_{Coll}} = \frac{160\ \text{mm}}{750\ \text{mm}} = 0.21, \quad (7)$$

TABLE IV. Geometric calibration session dataset.

Session name	VIHI parameters	OGSE configuration	Test description
CGNVACRASD	Int. time = 20.55 ms FPA T = 219.9 K	-Target: a 50 μm wide slit in the OGSE focal plane -No diffuser -VIS collimator -ASD illumination -Steering mirror: EL: −1.023 18° (−FOV/2), −0.415 91° (−FOV/4), 0.218 86° (boresight), 0.869 02° (+FOV/4), 1.385 69° (+FOV/2) AZ_{steps}: 60 steps of 0.000 716 2° (1/10 IFOV/step)	Slit function: −5 scans centered at different FOV positions with EL = boresight, ±FOV/2, ± FOV/4 −3 detector frames per step −3 background frames
CGNVALNASD	Int. time = 4.795 ms FPA T = 219.9 K	-Target: a 700 μm wide slit in the OGSE focal plane -No diffuser -VIS collimator -ASD illumination -Steering mirror: EL_{steps}: 130 steps of 0.001 013° (1/10 IFOV/step) EL_{start}: −1.055 1° (−FOV/2), −0.462 04° (−FOV/4), 0.168 785° (boresight), 0.822 345° (+FOV/4), 1.395 66° (+FOV/2) AZ: fixed at 43.418 95°	Pixel function-FOV: −5 scans centered at Different FOV positions with EL = boresight, ±FOV/2, ± FOV/4 −3 detector frames per step −3 background frames
CGNIALNASD	Int. time = 4.453 ms FPA T = 219.9 K	-Target: a 700 μm wide slit in the OGSE focal plane -No diffuser -IR collimator -ASD illumination -Steering mirror: EL_{steps}: 130 steps of 0.001 013° (1/10 IFOV/step) EL_{start}: −1.055 1° (−FOV/2), −0.462 04° (−FOV/4), 0.168 785° (boresight), 0.822 345° (+FOV/4), 1.395 66° (+FOV/2) AZ: Fixed at 43.418 95°	Pixel function-FOV: −5 scans centered at Different FOV positions with EL = boresight, ±FOV/2, ± FOV/4 −3 detector frames per step −3 background frames
CGNIUSAFHP	Int. time = 54.937 ms FPA T = 219.9 K	-Target: USAF/51 resolution mask in OGSE focal plane -Integrating sphere and QTH lamp illumination -Steering mirror: AZ_{start}: 43° AZ_{steps}: 110 steps of 0.007 162° (1 IFOV/step) EL: 0.230 32°	MTF scan across slit -Spatial scan to build image −10 frames/step −10 background frames

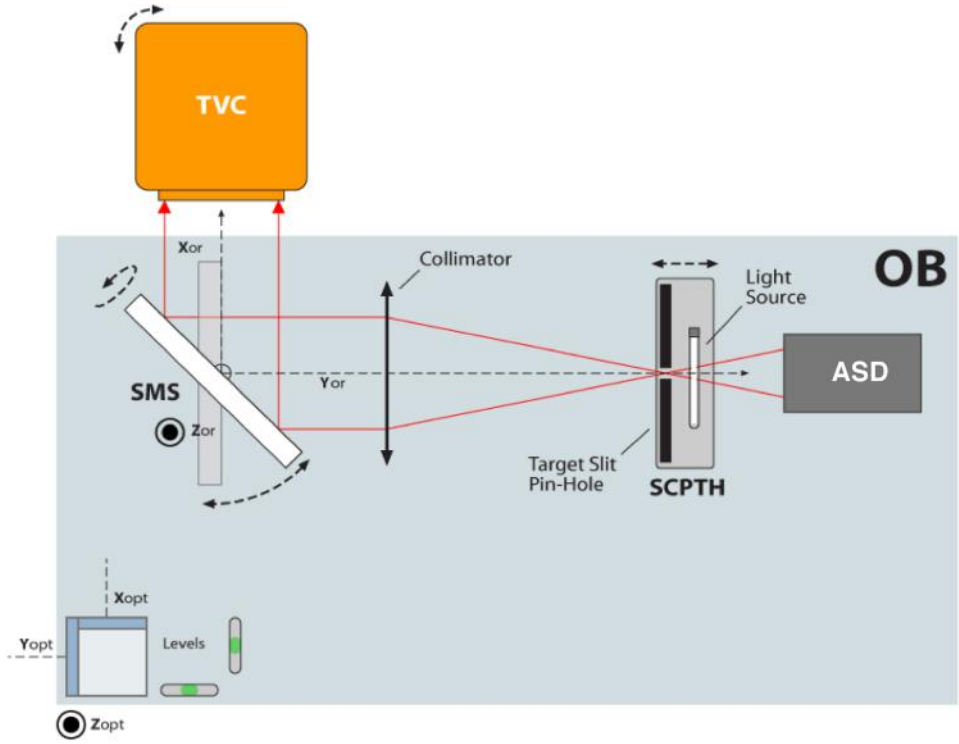

FIG. 19. VIHI geometrical calibration setup schematics. The target slit or the USAF mask illuminated by a light source is placed at the collimator's focus. The target is aligned and focused by means of the Autocollimating Sensing Device (ASD).

which means that an object of size D placed at the collimator focus is seen by VIHI with a dimension of $D \times MR$. The VIHI FOV is limited by the detector size (256 samples, 40 μm pixel size) and corresponds to a size of 4.876 cm on the collimator focal plane once the MR of the OGSE system is considered.

In Table IV, the datasets acquired with this setup are listed, which are detailed in Secs. XI–XII together with the algorithms used to process the data. In general, for each session of measurements, dark frames have also been acquired with the same integration times necessary to remove the dark current contribution from the signal.

IX. SLIT AND PIXEL FUNCTION MEASUREMENTS

Slit and pixel functions allow a characterization of the VIHI IFOV along the two spatial directions: in the slit function, the test slit is placed parallel to the VIHI slit during the scan while the pixel function is measured by means of a spatial scan of the test slit oriented perpendicular to the VIHI slit. In both cases, the test slit is moved at a subpixel step for each acquisition in order to oversample the angular resolution. A similar methodology has been applied to characterize the geometrical performances of other VIS-IR imaging spectrometers.[7,9] The slit width has been selected in order to ensure coverage of a significant number of pixels (≈4) along the VIHI slit in order to gain sensitivity in knife-edge detection, without affecting illumination uniformity. The source used to illuminate the slit is a miniaturized QTH lamp provided with a set of diffusers in order to improve uniformity. A sketch of the OGSE configuration during geometric calibrations is shown in Fig. 19 while the concept of the pixel and slit function scans is given in Fig. 20. Before each measurement, the SMS axes are referred to a repeatable (target-dependent) origin for AZ-EL coordinates. Moreover, the alignment of the target slit oriented parallel or orthogonal to the VIHI slit axis is implemented by manually rotating the target disk holder and checking interactively the acquired signal. The

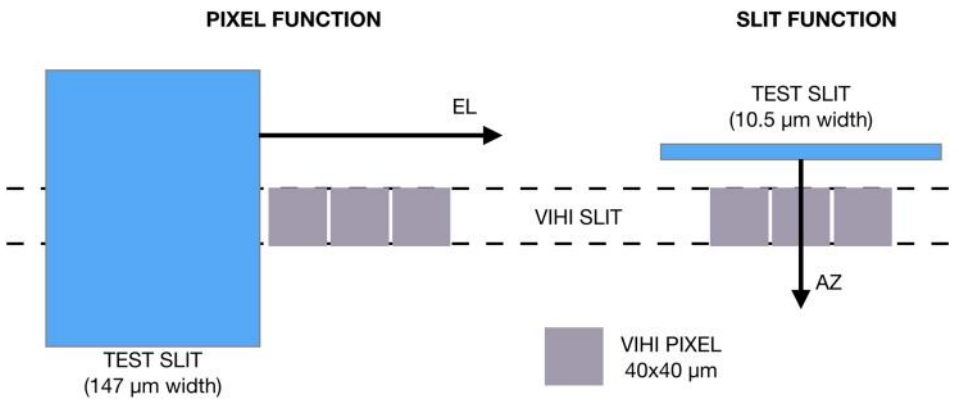

FIG. 20. Concept of pixel and slit function scans. The dimension of the test slits is scaled according to the MR [Eq. (7)].

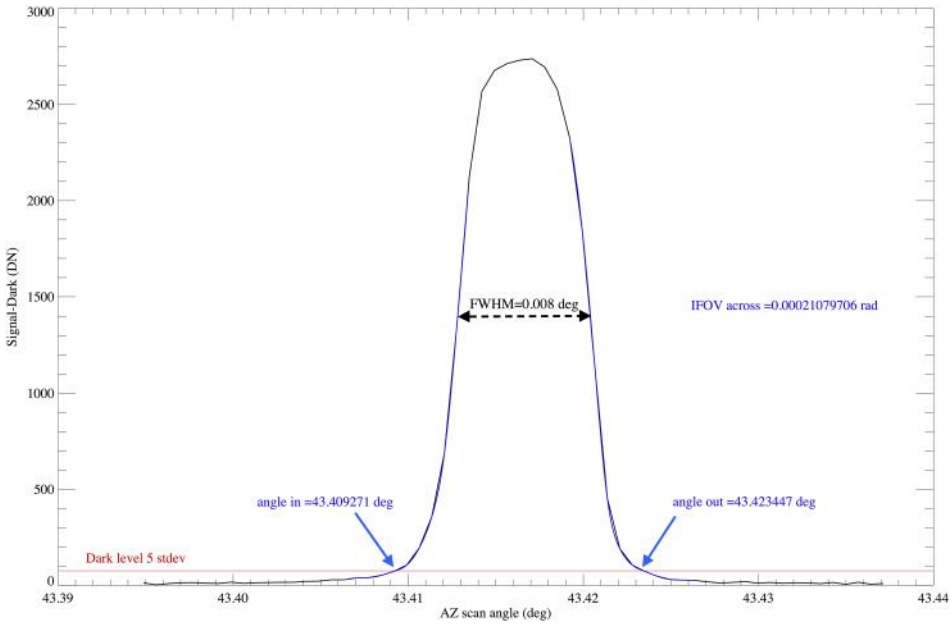

FIG. 21. Signal profile acquired during the slit function scan at boresight for band = 191 (black curve). The inbound and outbound ramps quadratic fits are shown (blue curves). The 5 standard deviation levels of dark current is marked by the red line. The positions of the AZ angles above the inbound and outbound ramps are indicated by the blue arrows, while the FWHM is marked in black.

optimization of the integration time setting occurs in the same context.

The *slit function* is measured by using a 50 μm wide test slit as a target placed parallel to the VIHI slit and is built in time by acquiring the signal for 60 steps, by incrementing the position of the test slit of 1/10 IFOV for step along the AZ angle. Since the optical beam passes through the collimator, the test slit is seen by VIHI with a size scaled by the MR factor [Eq. (7)] which reduced it to 10.5 μm ($\approx$1/4 pixel). As reported in Table IV at each step, a total of three frames are acquired and averaged in order to improve the signal to noise. The average dark current of the frames acquired at the beginning and end of the scan is then subtracted pixel by pixel. The scope of this measurement is to acquire the signal collected by a given pixel when it is sampled by a subpixel light source passing through it, e.g., moving from outside the FOV, reaching the pixel center position and then moving out. Each scan is repeated by moving the position of the test slit within the FOV: at boresight, FOV boundaries and intermediates. In order to measure the effective IFOV of the pixel, it is necessary to take into account the absolute azimuth (AZ) and elevation (EL) angles of the SMS corresponding to each step during the scan. As an example, we report the signal profile acquired at boresight for band = 191 in Fig. 21.

After having subtracted, the dark current from the signal is possible to study in detail the bell-shaped profile as a function of the SMS AZ angle. The experimental points taken along the inbound and outbound part of the curve are modeled with a quadratic fit. The AZ and EL angle values corresponding to the inbound and outbound fitted curves corresponding to 5 times the dark current standard deviation are used to infer the unit vectors that define the absolute direction in the space of the scan angle,

$$\begin{aligned} i &= \sin(2 \cdot AZ) \cdot \cos^2(EL) \\ j &= 1 - 2 \cdot \cos^2(AZ) \cdot \cos^2(EL) \\ k &= -\cos(AZ) \cdot \sin(2 \cdot EL). \end{aligned} \tag{8}$$

This method allows compensating for any residual non-parallelism between the test and VIHI slits during the scan. The IFOV across slit is therefore computed by means of the scalar product,

$$IFOV_{across} = a \cos(i_{in} \cdot i_{out} + j_{in} \cdot j_{out} + k_{in} \cdot k_{out}). \tag{9}$$

The results of the slit function (e.g., IFOV across slit) for five positions along the FOV (sample = 5, 64, 128, 194, 246) and at three spectral bands (B = 101, 151, 191) are reported in Table V. In some cases (B = 101, S = 128; B = 191, S = 194), the anomalous low values are caused by the presence of defective pixels on the detector. Uncertainty on the retrieved IFOV values is estimated in the order of 5%–10%.

Alternatively, the slit function can be estimated by measuring the FWHM of the signal profile shown in Fig. 21, which is equal to 0.008° = 140 μrad and corresponds to 56% of the pixel IFOV. Since this angle is measured along the AZ axis and is determined between two positions of the OGSE scan mirror, it must be multiplied by a factor $\times$2 to take into account the reflection on the surface of the SMS (see Fig. 19). With this method, the slit function is therefore equal to 280 μrad or 112% of the nominal IFOV. This excess is caused by residual aberrations in the optical system (the collimator spatial response enlarges the test slit image seen by VIHI) and by a not perfect parallelism between the two slits.

TABLE V. Slit spatial response functions for samples S = 5, 64, 128, 194, 246 at bands B = 101, 151, 191.

Sample no.	IFOV (μrad) at band = 101	IFOV (μrad) at band = 151	IFOV (μrad) at band = 191
5	245.5	232.3	235.5
64	227.5	219.8	219.8
128	154.2	246.3	212.4
194	243.1	227.7	98.5
246	233.2	240.0	241.3

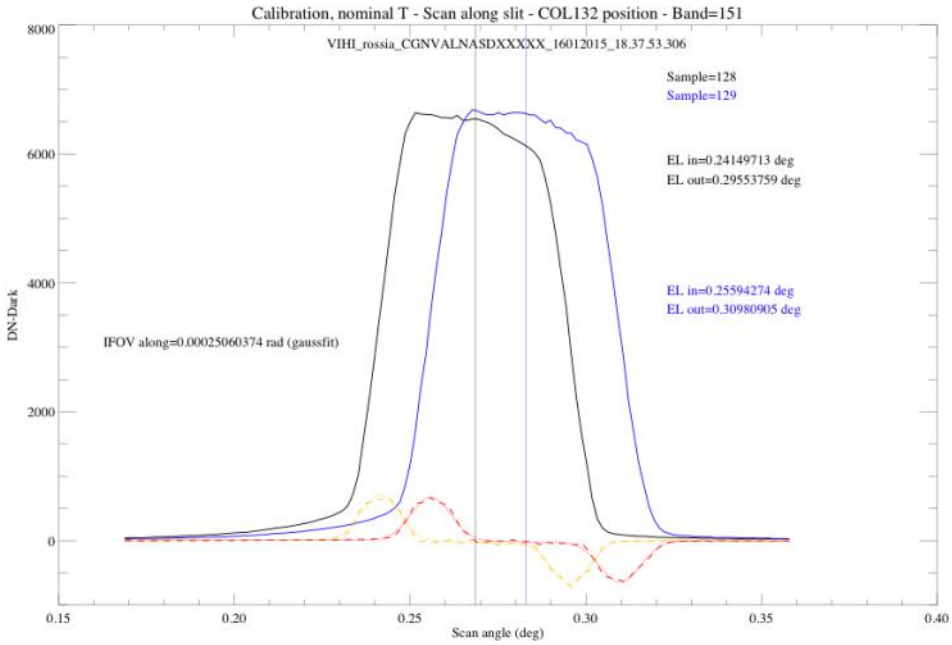

FIG. 22. Pixel function scan: signals acquired during the EL scan on pixels at (sample, band) = (128, 151) and (129, 151) (black and blue curves, respectively), their first derivative (yellow and red curves, respectively) and resulting pixel function widths.

The *pixel function* is measured by using as a target, a 700 μm wide test slit placed at the collimator's focal plane with an orientation perpendicular to the VIHI slit. After scaling for the MR [Eq. (7)], the test slit width seen by VIHI is 147 μm wide (≈3.7 pixels). The scan is built in time acquiring the signal for 130 steps, by incrementing the position of the test slit of 1/10 IFOV for each step along the EL angle scan. At each step, the absolute orientation of the scan angle in space has been computed by using the EL-AZ angles of the SMS through Eq. (8) to derive the unit vectors. From them, the following scalar product gives the absolute value of the scan angle α,

$$\alpha = a\ \cos(i(n)\cdot i(n+1) + j(n)\cdot j(n+1) + k(n)\cdot k(n+1)). \tag{10}$$

The large width of the test slit has been selected to optimize the signal at the knife edges but causes a not uniform profile near the maximum (see Fig. 22). Conversely, the determination of the IFOV depends on the position of the two inflection points computed on the inbound and outbound ramps, which can be computed by means of the first derivative. As an example, in Fig. 22, the scan profiles (after dark removal) measured on two contiguous pixels (samples 128 and 129, shown as black and blue curves, respectively) and the corresponding first derivative curves (yellow and red lines) are shown. The position of the two flex points on the derivative curve is computed as the center of the best fit gaussian curves taken on the inbound and outbound ranges. The difference between these two values, once converted in α following Eq. (10), gives the IFOV value. Each scan is repeated by moving the position of the test slit within the FOV: at boresight, FOV boundaries, and intermediate points. The pixel function FWHM values measured at different samples and bands are reported in Table VI for the VIS and IR collimators spectral ranges (bands = 151, 191, 225 and 5, 51, 101, respectively). Uncertainty on the retrieved IFOV values is estimated in the order of 5%–10%. Finally, the VIHI pixel function is unaffected by the detector filling factor that is 100%. The detector architecture guarantees the absence of any blind region between adjacent pixels. As a consequence of this, all incident photons are collected by the pixels and the ingress and egress signal ramps measured during the scans are not influenced by a similar effect.

TABLE VI. Results of the pixel function measurements along the slit. Measurements from session CGNVALNASD are used in the 0.4–1.0 μm VIS collimator spectral range (bands = 151, 191, 225) and from session CGNIALNASD in the 1.0–2.0 μm IR collimator spectral range (bands = 5, 51, 101).

Sample no.	IFOV (μrad) at band = 5	IFOV (μrad) at band = 51	IFOV (μrad) at band = 101
5÷6	258.2	256.2	253.4
65÷66	247.6	248.9	250.8
128÷129	254.3	254.1	252.5
195÷196	257.7	257.9	255.4
250÷251	256.0	253.3	250.4
Sample no.	IFOV (μrad) at band = 151	IFOV (μrad) at band = 191	IFOV (μrad) at band = 225
5÷6	254.7	253.4	254.8
65÷66	249.7	249.5	251.3
128÷129	250.6	254.6	252.7
195÷196	247.7	249.2	252.2
250÷251	253.3	255.5	254.6

X. FIELD OF VIEW CHARACTERIZATION

The determination of VIHI Field Of View (FOV) is performed by means of the same spatial scan used to determine the pixel function. In this case, the signal collected by pixels placed at samples = 2, 129, 255 and at band = 128 with the scope to determine the angular distance among them is analyzed. The measurement of the angle between samples 2 and 255 gives a

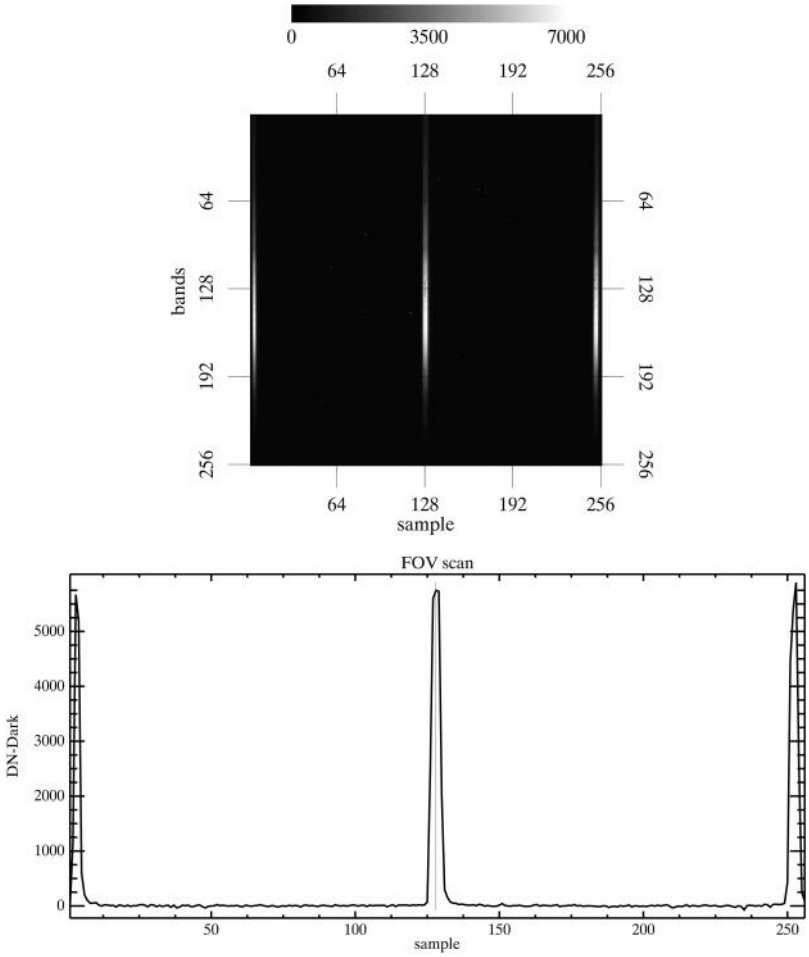

FIG. 23. Characterization of the VIHI FOV by means of spatial scan. Top panel: reconstructed frame showing the test slit signal during the spatial scan above samples 2, 129, 255. Bottom panel: dark subtracted signal at band = 128 showing the position of the three peaks at FOV edges and the boresight measured during the scan.

measurement of the full FOV extension while between samples 2–129 and 129–255 allows characterizing the angular distance of the two FOV extremes from the boresight. In this analysis, the first (sample = 1) and last (sample = 256) columns are not considered because at the edge of the detector, it is not possible to achieve a reliable reconstruction of the signal profile during the scan. In Fig. 23—top panel—shown is the reconstructed image of the three acquisitions of the illuminated slit during the scan taken in correspondence to the maximum signal above samples = 2, 129, 255. The bottom panel shows a profile of the reconstructed signal, dark subtracted, taken in correspondence to band = 128. The three peaks correspond to the slit signal acquired by VIHI during the scan on those pixels. The knowledge of the AZ-EL angles (Table VII) of the SMS reached during the scan in correspondence to the centers of the three peaks shown in Fig. 23—top panel—allows computing the unit vectors by means of Eq. (8). The scalar product α [given by Eq. (10)] between them corresponds to the FOV values reported in Table VIII. By dividing the number of samples within the FOV extremes and center, it is possible to estimate the average IFOV.

In conclusion, the total VIHI FOV measured across the samples 1÷256 can be estimated by multiplying 256 times the average IFOV measured between samples 2÷255. This corresponds to a value of FOV_{VIHI} = 256 × 246.8 μrad = 0.063 180 8 rad = 3.62°.

TABLE VII. Azimuth (AZ) and Elevation (EL) angles of the SMS corresponding to the center of samples s = 2, 129, 255.

Sample no.	AZ (rad)	EL (rad)
2	0.757 804	−0.017 724 4
129	0.757 803	0.003 830 78
255	0.757 805	0.025 260 4

XI. IMAGING TESTS AND MTF MEASUREMENT WITH USAF MASK

The Modulation Transfer Function (MTF) measures the capability of an optical system to register various levels of spatial frequencies from the object to the image and is given in units of the ratio between the image contrast and the object

TABLE VIII. FOV and average IFOV values measured between samples = 2÷255 and between boresight (s = 128) and FOV extreme positions (s = 2, 255).

Range	FOV (rad)	Avg. IFOV (μrad)
2÷255	0.062 433 8	246.8
2÷129	0.031 312 3	246.5
129÷255	0.031 128 9	247.1

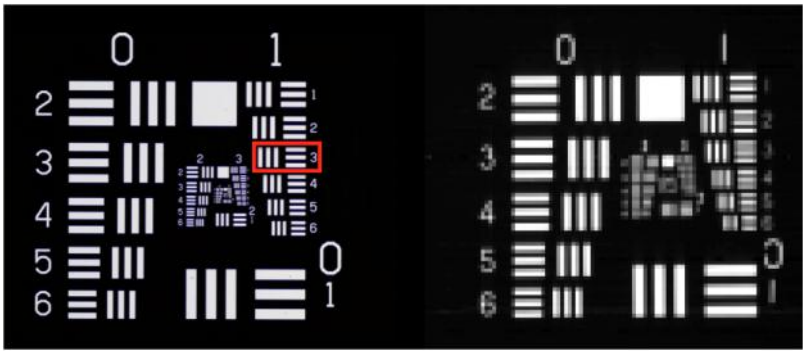

FIG. 24. Left panel: USAF mask 1951 reference image. The pattern G = 1, E = 3 indicated by the red box corresponds to VIHI theoretical $f_{Nyquist}$ = 2.6 lines/mm. Right panel: VIHI image of the mask at wavelength λ = 590 nm. The mask patterns (without external labels) are imaged on 64 × 64 pixels. The VIHI slit (sample direction) is oriented towards the vertical axis and the image is acquired in time by scanning along the horizontal axis of the image.

contrast as a function of the spatial frequency.[10] The measurement is performed by using a USAF 1951 resolution test target placed on the OGSE focal plane, illuminated in transmission by an integrating sphere to achieve an uniform beam. A QTH lamp, coupled to the integrating sphere by means of an optical fiber is used as a source. The target image is acquired by performing with the SMS an AZ scan (orthogonal to the VIHI slit) of 110 steps, at step equivalent to 1 IFOV, ensuring a coverage of the full angle subtended by the target as seen through the collimator. This test allows verifying VIHI focusing and optical performances: within the set of spatial frequencies available on the USAF target, the image quality at the Nyquist frequency can be checked.

The Nyquist frequency of VIHI observing through the collimator is given by

$$f_{Nyquist} = \frac{1}{2 \cdot d \cdot \frac{1}{MR}}, \tag{11}$$

where d = 40 μm is the VIHI detector pixel size and MR is the magnification ratio given by Eq. (7). Therefore, for the optical configuration used in the test, a $f_{Nyquist}$ = 2.6 lines/mm is reached. On the USAF 1951 mask, the frequency of the lines identified by the Group (G, along horizontal axis) and Element (E, along vertical axis) sets is given by the resolution equation,

$$f_{USAF} = 2^{(G+\frac{E-1}{6})}. \tag{12}$$

TABLE IX. Values of the signal statistics ($DN_{\max,\min}$) and derived contrast (C) measured on the USAF mask at different frequencies. The MTF values derived at $f_{Nyquist}$ = 2.52 lines/mm are shown in bold text.

	Across direction			Along direction		
Lines/mm	$DN_{\max}$	$DN_{\min}$	C	$DN_{\max}$	$DN_{\min}$	C
1.00	1199	22	0.96	1118	89	0.85
1.12	1163	52	0.91	1153	153	0.76
1.26	1173	38	0.94	1105	150	0.76
1.41	1167	84	0.87	1005	172	0.71
1.59	1042	141	0.76	1041	192	0.69
1.78	686	144	0.65	828	197	0.61
2.00	920	229	0.60	895	365	0.42
2.24	811	285	0.48	831	380	0.37
2.52	863	308	**0.47**	800	381	**0.35**
2.83	700	558	0.11	692	428	0.23
3.17	690	527	0.13	681	499	0.15

VIHI theoretical $f_{Nyquist}$ is achieved in correspondence to the G = 1, E = 3 pattern for which f_{USAF} = 2.52 lines/mm. The G = 1, E = 3 pattern is indicated on the reference image of the USAF mask shown in Fig. 24.

For each horizontal and vertical pattern of lines in Groups G = 0÷1 and Elements E = 1÷6, the contrast value (C) is computed as

$$C = \frac{DN_{\max} - DN_{\min}}{DN_{\max} + DN_{\min}} \tag{13}$$

after having subtracted the dark current and applied a flat field frame. The signal minimum and maximum values derived on the patterns and corresponding C values in the across and along directions are listed in Table IX. The VIHI MTF values computed at $f_{Nyquist}$ are equal to 0.47 and 0.35 in the across and along directions, respectively.

XII. CONCLUSIONS

This is Paper I of a series dedicated to the description of the pre-launch characterization of the VIHI hyperspectral imager, part of the SIMBIO-SYS payload onboard the Bepi-Colombo mission to Mercury. We have addressed here the radiometric and linearity calibration by means of a dedicated setup that is able to reproduce the expected radiance levels occurring during the different scientific phases of the mission. The instrument responsivity has been characterized for different combinations of integration times and input radiances, allowing us to verify the response at different levels of the dynamical range. The spatial homogeneity of the calibration source (an integrating sphere) has permitted us to measure the responsivity across the entire field of view, embedding the flat-field array within the Instrument Transfer Matrix (ITF). Apart from this, the linearity responses of the instrument signal and dark current have been determined for a wide range of integration times, input fluxes, and detector's temperatures. In average, the response is linear within a ±2% level across a wide dynamical range, with a worsening of the response only in correspondence to saturation and low signal levels. The dark current rate has been characterized within the range of detector's expected temperatures at operative conditions. The measured responsivity is used to simulate the expected signal from the surface of Mercury for four different Bepi-Colombo observation scenarios, allowing us to determine the signal to noise ratio that is satisfactory (≥100) for all the considered cases. The measurements of the instrumental pixel

and slit functions show that the geometric performances are satisfactory being the values of the FOV, IFOV, and MTF within the scientific requirements. These results give us the confidence that the instrument has been designed and assembled to fully meet the scientific requirements of the mission. Paper II[4] will address the spectral characterization of the VIHI spectrometer.

ACKNOWLEDGMENTS

The pre-launch calibration of the VIHI instrument has been realized under an Agenzia Spaziale Italiana (ASI) contract to the Istituto Nazionale di Astrofisica (No. INAF I/022/10/0) and with the technical and logistic support of Leonardo Company (Campi di Bisenzio, Florence, Italy) prime industrial contractor of the SIMBIO-SYS payload. This research has made use of NASA's Astrophysics Data System.

[1]E. Flamini, F. Capaccioni, L. Colangeli, G. Cremonese, A. Doressoundiram, J. L. Josset, Y. Langevin, S. Debei, M. T. Capria, M. C. de Sanctis, L. Marinangeli, M. Massironi, E. Mazzotta Epifani, G. Naletto, P. Palumbo, P. Eng, J. F. Roig, A. Caporali, V. da Deppo, S. Erard, C. Federico, O. Forni, M. Sgavetti, G. Filacchione, L. Giacomini, G. Marra, E. Martellato, M. Zusi, M. Cosi, C. Bettanini, L. Calamai, M. Zaccariotto, L. Tommasi, M. Dami, J.F. Veltroni, F. Poulet, Y. Hello, and SIMBIO-SYS Team, Planet. Space Sci. **58**, 125 (2010).

[2]H. Hayakawa, Y. Kasaba, H. Yamakawa, H. Ogawa, and T. Mukai, Adv. Space Res. **33**, 2142 (2004).

[3]F. Capaccioni, M. C. de Sanctis, G. Filacchione, G. Piccioni, E. Ammannito, L. Tommasi, I. F. Veltroni, M. Cosi, S. Debei, L. Calamai, and E. Flamini, IEEE Trans. Geosci. Remote Sen. **48**, 3932 (2010).

[4]F. Altieri, G. Filacchione, F. Capaccioni, C. Carli, M. Dami, L. Tommasi, G. Aroldi, A. Barbis, M. Baroni, G. Pastorini, and I. F. Veltroni, Rev. Sci. Instrum. **88**, 094503 (2017).

[5]V. Da Deppo, E. Martellato, G. Rossi, G. Naletto, V. Della Corte, F. Capaccioni, G. Filacchione, M. Zusi, P. Palumbo, G. Aroldi, M. Baroni, D. Borrelli, L. Tommasi, M. Dami, I. F. Veltroni, E. Flamini, and G. Cremonese, Proc. SPIE **9143**, 914344 (2014).

[6]G. Filacchione, "Calibrazioni a terra e prestazioni in volo di spettrometri ad immagine nel visibile e nel vicino infrarosso per l'esplorazione planetaria," Ph.D. thesis, Aerospace Engineering, Naples University Federico II, 2006.

[7]G. Filacchione, E. Ammannito, A. Coradini, F. Capaccioni, G. Piccioni, M. C. de Sanctis, M. Dami, and A. Barbis, Rev. Sci. Instrum. **77**, 103106 (2006).

[8]M. P. Thekaekara, Appl. Opt. **15**, 915 (1976).

[9]E. Ammannito, G. Filacchione, A. Coradini, F. Capaccioni, G. Piccioni, M. C. de Sanctis, M. Dami, and A. Barbis, Rev. Sci. Instrum. **77**, 093109 (2006).

[10]W. J. Smith, *Modern Optical Engineering* (McGraw-Hill, 2000).